https://doi.org/10.5194/egusphere-2025-4254
Preprint. Discussion started: 5 September 2025

Meteoric beryllium-10 fluxes from soil inventory measurements in the East River watershed, Colorado, USA

José M. Marmolejo-Cossío [1], Isaac J. Larsen[1,2], Alan J. Hidy[3]

[1]Department of Earth, Geographic, and Climate Sciences, University of Massachusetts, Amherst, 01003, USA
[2]Rocky Mountain Biological Laboratory, Crested Butte, CO, 81224, USA
[3]Center for Accelerator Mass Spectrometry, Lawrence Livermore National Laboratory, Livermore, CA, 94550, USA

Correspondence to: Isaac J. Larsen (ilarsen@umass.edu)

Abstract. Meteoric beryllium-10 ($^{10}Be_{met}$) has a wide range of applications as a geochronometer and tracer of geological processes. $^{10}Be_{met}$ is produced in the atmosphere by cosmic rays and delivered to Earth's surface primarily via precipitation. $^{10}Be_{met}$ is particularly suitable for quantifying surface process rates where use of *in situ*-produced ^{10}Be is challenging, such as landscapes with quartz-poor bedrock. However, using $^{10}Be_{met}$ for dating and quantifying surface process rates requires constraining depositional fluxes across space and time. Although empirical and physical models for predicting fluxes exist, the predictions can deviate substantially from measured values. Here we quantify $^{10}Be_{met}$ flux in the East River watershed in Colorado, USA where precipitation is dominated by snowfall. We measured the $^{10}Be_{met}$ inventory in soils on five glacial moraines 13–18 ka in age that span 700 m of elevation and calculated $^{10}Be_{met}$ fluxes by dividing each inventory by moraine age. Inheritance-corrected fluxes range from 1.12×10^6–3.79×10^6 atoms cm^{-2} yr^{-1}, and are well correlated with elevation, mean annual precipitation, mean snow depth, and snow water equivalent ($R^2 = 0.84$ to 0.99). Regression models based on elevation, precipitation, snow depth and snow water equivalent predict watershed-averaged fluxes of 1.23×10^6–3.62×10^6 atoms cm^{-2} yr^{-1}. Predicted fluxes from a published empirical model that estimates fluxes as a function of precipitation were within a factor of 1.1–1.6 of measured values at each site. Fluxes predicted by physically-based general circulation models (GCM) are generally within a factor of three of our estimated watershed-averaged values, but the GCM predictions are too coarse to capture the intra-watershed spatial variability in fluxes. Our results highlight both the importance of factors that drive variability in $^{10}Be_{met}$ delivery to soils and how local calibration can improve estimates of $^{10}Be_{met}$ flux in mountain watersheds.

1 Introduction

The cosmogenic nuclide beryllium-10 (^{10}Be) is used widely for geochronology and to quantify rates of Earth surface processes (Bierman and Nichols, 2004; Willenbring and von Blanckenburg, 2010). ^{10}Be forms during high energy collisions between cosmic particles and target nuclei (Lal and Peters, 1967). ^{10}Be produced in Earth's atmosphere (typically from N and O) is known as atmospheric, garden variety, or meteoric ^{10}Be ($^{10}Be_{met}$), whereas *in situ*-produced ^{10}Be ($^{10}Be_{in\ situ}$) is formed in mineral lattices at and near Earth's surface. Production rates of $^{10}Be_{in\ situ}$ are on the order of a few to tens of atoms g^{-1} yr^{-1} in quartz

(Gosse and Phillips, 2001; Borchers et al., 2016). In contrast, $^{10}\mathrm{Be}_{\mathrm{met}}$ is generated at orders of magnitude higher rates, with global-averaged values in excess of one million atoms cm^{-2} yr^{-1} (Monaghan, et al., 1986; McHargue and Damon, 1991). $^{10}\mathrm{Be}_{\mathrm{met}}$ is circulated throughout the atmosphere before being removed through precipitation or dry fallout (Field 2006; Heikillä et al., 2008). Once delivered to Earth's surface, $^{10}\mathrm{Be}_{\mathrm{met}}$ binds with minerals within soil, and is preferentially adsorbed to the surfaces of fine-grained particles and secondary minerals (e.g., Graly et al., 2010). $^{10}\mathrm{Be}_{\mathrm{met}}$ is partitioned with the solid phase for approximately neutral pH values (You et al., 1989) and is generally thought to be retained in soils where pH is > ~4 (Graly et al., 2010). However, $^{10}\mathrm{Be}_{\mathrm{met}}$ may be lost from upper soil horizons where low pH leads to leaching (Dixon et al., 2018), where clays or humic material with adsorbed Be are translocated to greater depth (Pavich et al., 1984; Jagercikova et al., 2015), and where the surface of the soil has been eroded (Harden et al., 2002). Hence soil $^{10}\mathrm{Be}_{\mathrm{met}}$ inventories depend on a variety of factors, including the local delivery rate, landform age, degree of chemical weathering, and erosion rate (e.g., Graly et al., 2010; Willenbring and von Blanckenberg, 2010).

The high production rates, which allow $^{10}\mathrm{Be}_{\mathrm{met}}/^{9}\mathrm{Be}$ ratios to be readily measured via accelerator mass spectrometry (AMS), the wide range of soils and regolith where $^{10}\mathrm{Be}_{\mathrm{met}}$ is retained, and – unlike $^{10}\mathrm{Be}_{in\ situ}$ – the ability to be measured in non-quartz-bearing materials has allowed $^{10}\mathrm{Be}_{\mathrm{met}}$ to be used widely as a geochronometer and tracer of Earth surface processes (e.g., Brown et al., 1987a; Graley et al., 2010; Willenbring and von Blanckenburg, 2010). For example, $^{10}\mathrm{Be}_{\mathrm{met}}$ has been used to date terraces and moraines (Tsai et al., 2018; Elgi et al., 2010; Dünforth et al., 2012), determine rock-to-soil production rates (Monaghan et al., 1992; McKean et al., 1993; Jungers et al., 2009), quantify soil residence times (Monaghan et al., 1983; Bacon et al., 2012; Foster et al., 2015), determine earthflow velocities (Macky et al., 2009), trace sediment through hillslopes and fluvial systems (Brown et al., 1988; Ruesser and Bierman, 2010; Campforts et al., 2016), and, when coupled with $^{9}\mathrm{Be}$ measurements, to quantify watershed-scale denudation rates and chemical weathering (von Blanckenburg et al., 2012; 2014; Dannhaus et al., 2018; Portenga et al., 2019; Deng et al., 2020a; 2021). However, a requirement for using $^{10}\mathrm{Be}_{\mathrm{met}}$ for dating and quantifying surface process rates is that the deposition rate or flux of $^{10}\mathrm{Be}_{\mathrm{met}}$ (F_{met}, atom cm^{-2} yr^{-1}) to the study area is known.

1.1 Quantifying the $^{10}\mathrm{Be}_{\mathrm{met}}$ flux

Numerous efforts have been made to measure or predict F_{met} at local to global spatial scales and over annual to millennial timescales (Willenbring and von Blanckenburg, 2010; Graly et al., 2011). Direct measurement of $^{10}\mathrm{Be}_{\mathrm{met}}$ concentrations in precipitation has been used to quantify $^{10}\mathrm{Be}_{\mathrm{met}}$ flux at point scales and short timescales to develop empirical relations that predict F_{met} as a function of precipitation rate or latitude (Brown et al., 1989; Monaghan et al., 1986; Raisbeck et al., 1981; Graham et al., 2003; Graly et al., 2011; Willenbring and von Blanckenburg 2010). Global-scale values of F_{met} are predicted with nuclide production functions (e.g., Lal and Peters, 1967; Masarik and Beer, 1999) that are coupled with general circulation models (GCM) to simulate spatial and temporal patterns of F_{met} as a function of geomagnetic field strength, solar activity, atmospheric circulation, and precipitation (Field et al., 2006; Heikillä et al., 2008; Heikillä and von Blanckenberg, 2015; Panovska et al., 2023; Zheng et al., 2021; Zheng et al., 2024). Millenial-averaged values of F_{met} can be inferred from soils by first measuring the ^{10}Be$_{met}$ inventory (I_{met}, atom cm^{-2}), which is typically done by multiplying the measured ^{10}Be$_{met}$ concentration (N, atom g^{-1}), by soil bulk density (ρ, g cm^{-3}) and the thickness of the sampling interval (z, cm), and summing the values for all (n) individual sample depth increments (i):

$$I_{met} = \sum_{i=1}^{n}(N \cdot \rho \cdot z)_i \tag{1}$$

Provided the landform age is much less than the mean life of ^{10}Be, the I_{met} value measured on an independently dated landform is then divided by age (t, yr),

$$F_{met} = \frac{I_{met}}{t}\,, \tag{2}$$

to determine the flux (e.g., Reusser et al., 2010; Ouimet et al., 2015; Clow et al., 2020; Graly et al., 2010). F_{met} values inferred from inventory measurements have been used to develop empirical models for relating flux to precipitation or latitude, similarly to precipitation-based flux measurements (Willenbring et al., 2010; Graly et al., 2011).

Using soil inventories to quantify F_{met} assumes that ^{10}Be$_{met}$ accumulation begins at the time a landform is initially exposed to wet and dry fallout. However, the ages of most landforms used to constrain flux are late Quaternary in age, or 1-2 orders of magnitude lower than the ^{10}Be half-life (1.387 Ma; Chmeleff, et al., 2010; Korschinek et al., 2010). Hence most soil inventories contain inherited ^{10}Be$_{met}$ atoms that were adsorbed to sediment grains prior to their incorporation within terraces and moraines (Graly et al., 2011). The inherited component can be identified by the presence of a near constant ^{10}Be$_{met}$ concentration in the lower part of a measured depth profile and once identified, can be subtracted from measurements at shallower depth to determine inheritance-corrected inventories (e.g., Reusser et al., 2010).

An additional assumption required to calculate F_{met} from soil inventories is that all ^{10}Be$_{met}$ delivered to the soil since landform initiation has been retained (Willenbring and von Blanckenburg 2010). Potential for ^{10}Be$_{met}$ loss due to chemical leaching can be assessed by measuring soil pH values. Potential loss of ^{10}Be$_{met}$ due to physical erosion can be minimized by selection of stable, flat surfaces for sampling. However, if the surface erosion rate is independently known, F_{met} can be determined for eroding landforms, provided the ^{10}Be$_{met}$ concentration in eroded material is also known (Brown, 1987b; Clow et al., 2020).

Soils contain ^{10}Be$_{met}$ scavenged from the atmosphere by aerosols, but also from dust particles that are derived from aeolian erosion and transported in the atmosphere before being deposited (Monaghan et al., 1986; Graly, 2011). The dust-derived or ‘recycled’ ^{10}Be$_{met}$ can be as much as ~20% of the total flux (Monaghan et al., 1986; Graham et al., 2003) and must be accounted for before comparing measured fluxes against predictions from general circulation models. However, the dust contribution to flux estimates does not need to be independently known to quantify surface process rates, provided that time-averaged delivery of dust to soils is representative of the timescale relevant to the surface process rate under investigation.

There is often disagreement between F_{met} values determined from soil inventories and global-scale physical models or empirical models that predict flux as a function of precipitation or latitude (Ouimet et al., 2015; Deng et al., 2020b; Krone et al., 2024). Substantial variability in F_{met} has been documented at spatial scales smaller than the grid cell size (often ~200 x 200 km) of many GCMs (Ouimet et al., 2015; Clow et al., 2020; Deng et al., 2020b). The discrepancies and spatial variability likely stem from temporal and spatial fluctuations in ^{10}Be$_{met}$ production, atmospheric circulation, and precipitation (Monaghan et al., 1986; Graham 2003; Jordan et al., 2003; Deng et al., 2020a; Krone et al., 2024). Hence, it is often desirable to locally-calibrate F_{met} prior to using ^{10}Be$_{met}$ to quantify surface process rates (e.g., Reusser et al., 2010; Ouimet et al., 2015). Local-scale calibration is particularly important in mountainous settings, where microclimate variability can cause ^{10}Be$_{met}$ inventories and fluxes to vary over short distances (Ouimet et al., 2015). Here we quantify the ^{10}Be$_{met}$ flux at sites throughout the East River watershed, near Crested Butte, Colorado, USA (Figure 1), a site of intensive research on the physical and biogeochemical drivers of watershed function (Hubbard et al., 2018). We measure ^{10}Be$_{met}$ inventories on independently dated glacial moraines, assess local-scale influences on ^{10}Be$_{met}$ flux, and compare ^{10}Be$_{met}$ flux measurements against predictions from empirical and physical models to evaluate the spatial variability and predictability of F_{met} values in alpine environments.

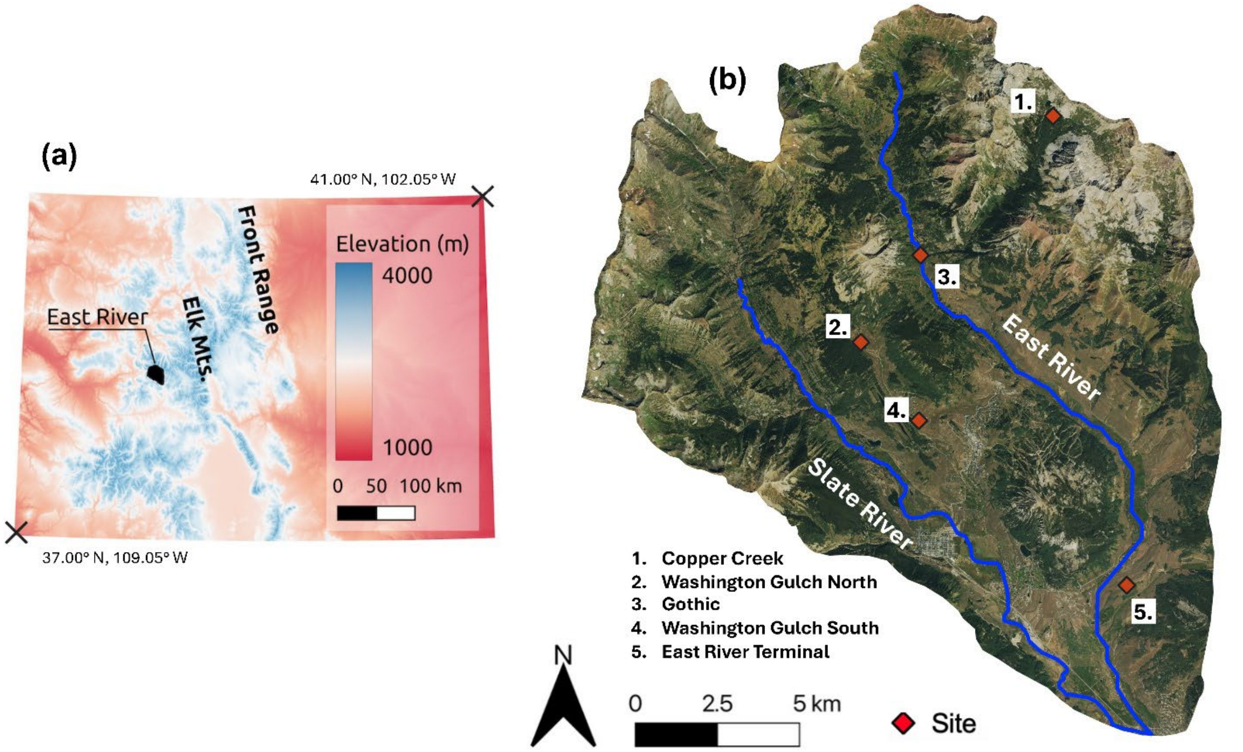

Figure 1: a) Digital elevation model (DEM) of Colorado, USA showing the location of East River watershed. b) True color (RBG) composite image of the East River watershed showing locations (red diamonds) where soil $^{10}Be_{met}$ inventories and fluxes were measured. The numbers show the location of each glacial moraine that was sampled: 1. Copper Creek; 2: Washington Gulch North; 3. Gothic; 4. Washington Gulch South; 5. East River terminal.

2 Study Site

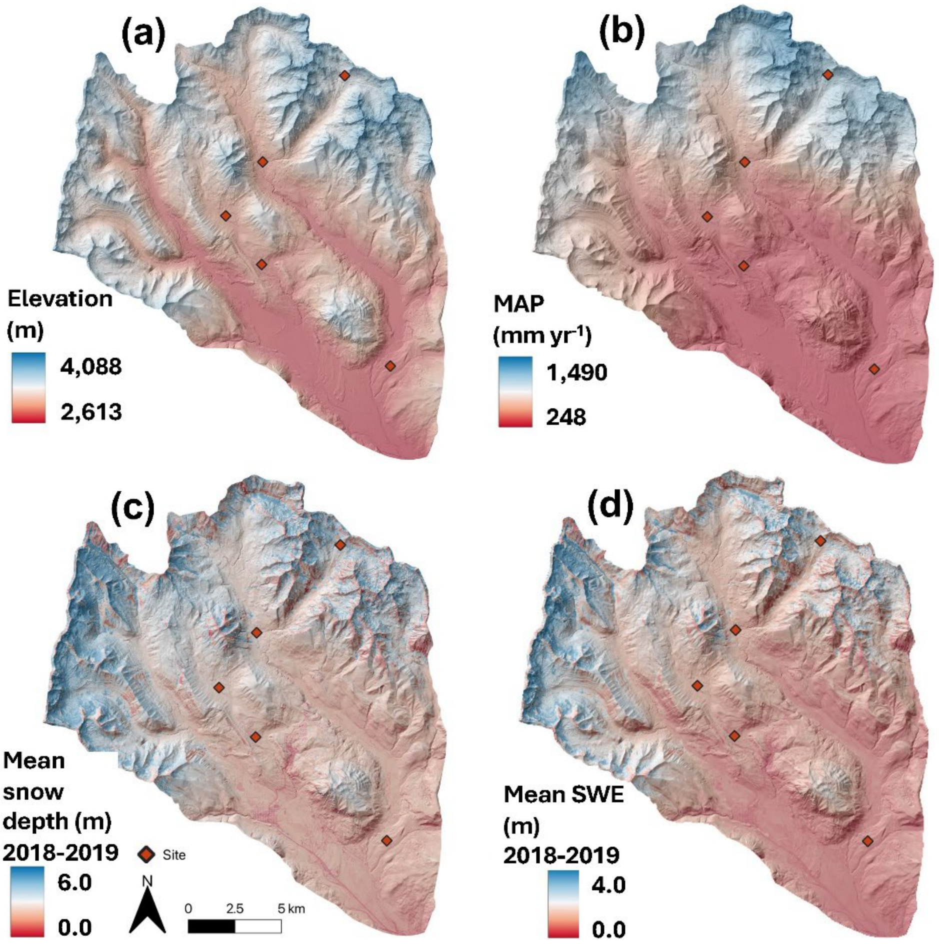

Figure 2: Maps of environmental variables within the East River watershed. (a) LiDAR-derived elevation data; (b) Mean annual precipitation (MAP) averaged from 2008–2019; (c) Mean snow depth, and (d) Mean snow water equivalent (SWE), derived from Airborne Snow Observatory data from 2018–2019. Red diamonds show locations of soil pits sampled to determine meteoric ^{10}Be inventories.

The East River drains the Elk Range of the Rocky Mountains in Colorado, USA (~38.9°N, 106.9°W). The East River joins the Taylor River to form the Gunnison River, a major tributary to the Colorado River. The East River watershed and its tributaries, Washington Gulch and the Slate River, are a steep mountainous landscape, with elevations that range from 2600 m to 4100 m above sea-level (Figure 2a). The climate is characterized by long, cold winters and cool, short summers (Hubbard et al., 2018). The mean annual temperature is ~0 °C, with mean minimum and maximum temperatures of -9.2 and 9.8 °C, respectively (Hubbard et al., 2018). Most of the annual precipitation occurs as snowfall, which can exceed several meters per year (Prather et al., 2023) and varies with elevation (Figure 2). The continental subarctic climate in the East River watershed supports montane, subalpine, and alpine ecosystems, which host aspen, meadow, mixed conifer, sagebrush, grass, sedge, and forb species (Figure S1) (Harte and Shaw, 1995). Bedrock in the watershed is primarily Cretaceous-age Mancos Shale and Paleocene to Miocene-age quartz monzonite porphyry and granodiorite intrusive rocks (Gaskill et al., 1967, 1991). Pleistocene glaciers eroded high elevation cirques and deposited moraines and outwash in the main East River valley (Gaskill et al., 1967, 1991). Exposure ages based on $^{10}\mathrm{Be}_{\textit{in situ}}$ concentrations measured in samples from boulders indicate the terminal moraine at the end of the valley dates to 17.9 ka, whereas the youngest recessional moraine in a high elevation cirque within the Copper Creek watershed was exposed at 13.0 ka (Quirk et al., 2024).

3 Methods

3.1 Field and laboratory methods

Soil $^{10}\mathrm{Be}_{\mathrm{met}}$ inventories were determined for five glacial moraines with exposure ages that range from 17.9 to 13.0 ka (Figure 1; Table 1; Quirk et al., 2024). Soil pits were dug on the flattest part of each moraine crest to minimize the potential of post-depositional erosion, with the exception of the Gothic moraine site, which was opportunistically located where the East River had laterally eroded a cutbank into the moraine, permitting deeper sampling. The pits were dug until shovel refusal, to depths between 50 and 175 cm. At the Washington Gulch North site, we sampled from a soil pit on a flat portion of the moraine, and collected a sample on the same moraine that was exposed by a recent landslide ~375 m from the soil pit to assess inheritance in a deeper sample than we could access by digging. Samples were collected in either 5 or 10 cm depth increments by pressing a stainless-steel box, open at the top and front, into the face of the soil pit and scraping soil into the box. Samples were dried and sieved to separate <2 mm particles. Splits of the <2 mm size fraction from multiple depth intervals were combined in proportion to the total mass of <2 mm particles in each sampling interval and powdered using a tungsten carbide shatter box. We measured soil pH to assess $^{10}\mathrm{Be}_{\mathrm{met}}$ retention by first mixing ~5 g of powdered <2 mm grain-size material with 12 mL ultrapure water. Samples were stirred and left overnight prior to measurements with a pH probe.

Table 1. Age and location of the calibration sites used to assess meteoric ^{10}Be flux.

Moraine	Age[a] ka	Latitude	Longitude	Slope[b] (°)	Curvature[c] (m^{-1})
Copper Creek	13.0±0.1	39.00119	-106.9401708	7.0	0.00
Washington Gulch North	17.9±0.2	38.9309257	-107.0133922	2.0	-0.03
Gothic moraine	15.0±0.1	38.9578776	-106.9908142	4.3	-0.04
Washington Gulch South	17.3±0.1	38.9073943	-106.9900578	0.5	-0.01
East River terminal	17.8±0.2	38.858632	-106.9075158	4.0	-0.02

[a] See Quirk et al. (2024) for exposure age details. [b] Slope (°) was generated using 3-meter LiDAR DEM (Wainwright and Williams). [c] Curvature (m^{-1}) was derived from a 1 m LiDAR DEM by fitting a polynomial surface to a neighbourhood of 11 pixels using LSDtopotools (Mudd et al., 2014).

$^{10}Be_{met}$ chemistry was conducted at the University of Massachusetts Cosmogenic Nuclide Laboratory using the Stone (1998) fusion method. Approximately 0.5 g of the homogenized and pulverized <2 mm soil particles was weighed into 30 mL Pt crucibles. We then added ~350 µg of ^{9}Be from a carrier with a $^{10}Be/^9Be$ ratio of $1.75x10^{-15}$ to each sample. We also added 1000 µg of Al from a commercial carrier, which reportedly improves Be yields (Stone and Balco, 2004). Samples were dried overnight at 60°C, then mixed with ~2.5 g of KHF_2 and ~0.5 g of $NaSO_4$ flux prior to heating with a gas torch to melt the sample. Once the samples were fully melted, they were heated for an additional 1-2 minutes. Be was extracted by soaking the crucibles with the fusion cakes overnight in 200 ml of ultrapure water. The solution was reduced to a volume of ~30 ml by evaporation, then centrifuged. We decanted the supernatant and added ~10–15 mL of 49% $HClO_4$ to precipitate K as $KClO_4$. The solution was centrifuged to remove $KClO_4$ and the supernatant was dried overnight in Teflon beakers following addition of 1 ml of 8M HNO_3. The samples were redissolved in 25 ml ultrapure water and Be was precipitated as BeOH by adding drops of ~10% NH_4OH until the solution pH was ~9. The BeOH was washed multiple times by repeatedly centrifuging, pouring off the supernatant, and remixing the BeOH with ultrapure water. The BeOH was dissolved with 2-3 drops 6M HCl, dried overnight in a quartz crucible, calcined by heating with a gas torch until BeO glowed orange for 1 minute, and packed into cathodes with Nb powder. The $^{10}Be/^9Be$ ratios were analyzed by AMS at Lawrence Livermore National Laboratory (LLNL) against AMS Be standard 01-5-4 (LLNL standard 07KNSTD) (Nishiizumi et al., 2007). ^{10}Be concentrations in soil samples were corrected by subtracting $^{10}Be/^9Be$ ratios measured in full process blanks from ratios measured in samples, with uncertainties added in quadrature.

3.2 $^{10}Be_{met}$ inventory and flux analysis

We calculated $^{10}Be_{met}$ concentrations assuming a bulk density value of 1.9 g cm^{-3}, based on prior measurements of glacial till within the valley (Quirk et al., 2024) and summed the concentrations from each depth interval to determine I_{met} for each site following equation 1. We then calculated an inheritance-corrected inventory (I_{cor}). At four of the five sites, the $^{10}Be_{met}$

concentration reached a near-constant value with depth (Figure 3). We assumed the concentration measured in the lowest depth interval was equal to the inherited ^{10}Be$_{met}$ concentration and subtracted that value from concentrations measured in overlying samples (e.g., Ruesser et al., 2010). At the fifth site in the Copper Creek watershed, the ^{10}Be$_{met}$ profile is well-mixed above a well-developed stone line at the base of the soil (Figure 3a). Hence, we used the mean inheritance value of 0.80x10^{8} atoms g^{-1} measured at the other four sites to correct for inheritance at the Copper Creek site. The 1σ uncertainty in I_{met} values was calculated by adding the AMS analytical uncertainty for individual depth increments in quadrature.

Inheritance-corrected F_{met} values were calculated using equation 2, assuming no erosion. Uncertainty in F_{met} for each calibration site was calculated by adding uncertainty in I_{met} values and moraine age in quadrature. Moraine age uncertainty was based on the standard error of the mean of multiple exposure ages or, for the Gothic Moraine, uncertainty associated with a ^{10}Be$_{in\ situ}$ depth profile age, as reported by Quirk et al. (2024).

The ^{10}Be$_{in\ situ}$ depth profile method used to date the Gothic moraine, which was also sampled for ^{10}Be$_{met}$, yielded a median erosion rate of 0.023 mm yr^{-1} (Quirk et al., 2024). The source area for the Gothic moraine is primarily intrusive rock and the till matrix hence contained sufficient quartz for ^{10}Be$_{in\ situ}$ analysis. However, at the other sites, the till matrix was dominated by quartz-poor Mancos shale and because of the dense shale-derived matrix, the pits could not be excavated deep enough to permit using a ^{10}Be$_{in\ situ}$ profile to assess erosion rates. Due to uncertainty in extrapolating the erosion rate from the Gothic Moraine to the other sites, we do not explicitly correct F_{met} values for erosion. However, we assessed the potential magnitude of the influence of erosion on fluxes (F_{cor_ε}) as:

$$F_{cor\_\varepsilon} = F_{met} + (\varepsilon \cdot N_{surface}) + (I_{met} \cdot \lambda) \tag{3}$$

where ε is the erosion rate (g cm^{-2} yr^{-1}), $N_{surface}$ is the ^{10}Be$_{met}$ concentration in the uppermost sample, and λ is the ^{10}Be decay constant, calculated as $\lambda=\ln(2)/t_{1/2}$. We modeled ε using values ranging from 0 to 0.04 mm yr^{-1} to encompass the range of possible median erosion rates (0.016–0.036 mm yr^{-1}) inferred from the ^{10}Be$_{in\ situ}$ depth profile at the Gothic moraine (Quirk et al., 2024). For low-gradient hillslopes like the moraines we sampled, erosion rates (ε) scale linearly with topographic curvature,

$$\varepsilon = \frac{dz}{dt} = D\nabla^2 z, \tag{4}$$

where dz/dt is the change in elevation (z) per unit time (m yr^{-1}), D is the topographic diffusion coefficient (m^{2} yr^{-1}), and ($\nabla^2 z$) is topographic curvature (m^{-1}) (e.g., Kwang et al., 2022). Given the similar materials and climate we assume D is comparable across the five moraines and based on differences in topographic curvature (Figure S2), calculated using

LSDTopoTools (Mudd et al., 2014), we assess whether the erosion rate at the Gothic moraine is representative of the other sites.

We used gridded datasets and univariate regression to assess the correlation between F_{met} and environmental variables: elevation, mean annual precipitation (MAP), snow depth, and snow water equivalent (SWE) (Table 2). The influence of elevation was evaluated using 3-meter resolution LiDAR data (Wainwright and Williams, 2017). We determined MAP at each site using downscaled (400 x 400 m) Parameter-elevation Regressions on Independent Slopes Model (PRISM; Daly et al., 2008) data from 2008–2019 (Mital et al., 2022), and snow data products derived from the Airborne Snow Observatory (ASO; Painter et al., 2018a, b). ASO combines airborne LiDAR and imaging spectrometry with snow energy balance models to generate spatially continuous snow data. Snow depth is calculated as the difference between a snow-covered LiDAR survey and a snow-free "bare-earth" LiDAR scan. For this study, we used ASO-derived snow depth data (3 m resolution) acquired on March 31, 2018, and April 7, 2019 (Painter et al., 2018a; Deems, 2019). Where data were absent in both years, snow depth was estimated from an elevation-based regression (Deems, 2019). We used SWE data (50 m resolution) from four dates: March 31 and May 24, 2018, and April 7 and June 10, 2019 (Painter et al., 2018b). To reduce the influence of temporal variability, we calculated the mean of the 2018 and 2019 snow depth and SWE datasets (Figure S3). We used the coefficient of determination (R^2) from linear regression analysis to assess the degree variability in F_{met} is explained by elevation and precipitation metrics. The significance of each regression model was determined using the associated p-value. For the precipitation-based metrics, we additionally calculated regression relationships with the y-intercept forced to be zero, because F_{met} should be zero where precipitation is zero, assuming dry fallout of $^{10}\mathrm{Be}_{\mathrm{met}}$ is negligible. We also predicted F_{met} for each of the five calibration sites using the precipitation-based empirical model of Graly et al. (2011) using the down-scaled PRISME MAP data (Mital et al., 2022) compared the predictions against the measured fluxes.

Using the linear regression parameters, we used the gridded elevation and precipitation datasets to generate spatially continuous predictions of F_{met} across the East River watershed, including the Washington Gulch and Slate River tributaries. We used the regression relationships with a forced y-intercept of zero to generate predictions based on MAP, snow depth, and SWE to ensure model predictions were physically plausible. We calculated the watershed-averaged flux predicted by elevation, MAP, snow depth, and SWE and compared those predictions against GCM-based predictions (Heikkilä and von Blanckenburg, 2015; Zheng et al., 2024).

4 Results

4.1 Soil pH

Soil pH for the uppermost sample interval of each profile ranged from 4.3–6.3 and generally increased with depth (Figure 3; Table S2). Mean pH values averaged across all depths for Copper Creek, Washington Gulch North, Gothic, Washington Gulch

South, and East River Terminal moraines are 4.7, 5.6, 5.7, 5.9, and 6.3, respectively. The most acidic soils are found at the Copper Creek moraine site, which is the highest elevation and is dominated by spruce-fir forest vegetation (Figure S1), where the lowest pH value of 4.3 was measured in the 0 to 10 cm depth increment.

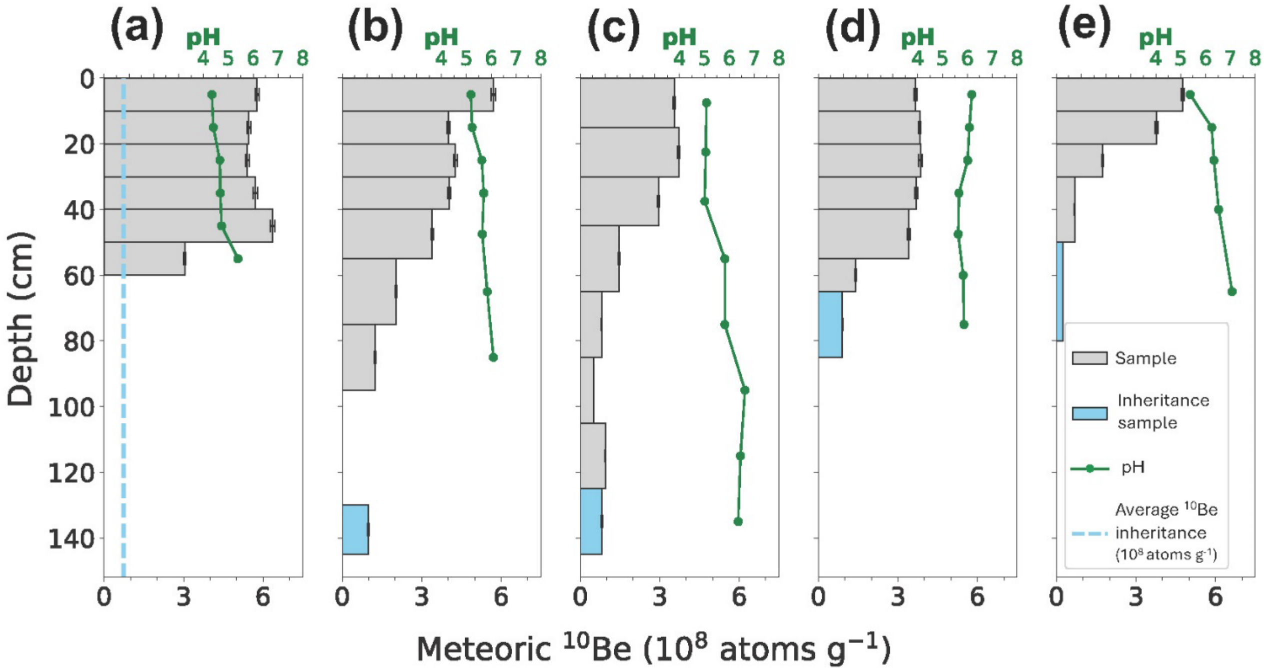

Figure 3. ^{10}Be$_{met}$ concentration and pH as a function of depth for (a) Copper Creek, (b) Washington Gulch North, (c) Gothic, (d) Washington Gulch South, and (e) East River Terminal moraines. Grey boxes show measured concentrations and uncertainties. Blue boxes indicate samples assumed to represent the inherited ^{10}Be$_{met}$ concentration. In (a), the blue dashed line shows the mean inheritance value calculated from profiles (b)–(e). The sample used for the inheritance correction in (b) was sampled from a landslide exposure on the Washington Gulch North moraine that was 374 m away from the soil pit where the other samples were collected.

4.2 ^{10}Be$_{met}$ profiles, inventories, fluxes, and controls on fluxes

^{10}Be/^{9}Be ratios typically were on the order of 1 to 10x10^{-12}, which is several orders of magnitude greater than the 10^{-15} ratios measured in blanks.Measured ^{10}Be$_{met}$ concentrations ranged from about 2.4x10^{7} to 6.4x10^{8} atom g^{-1} (Table 2). The ^{10}Be$_{met}$ concentration profiles exhibit a variety of shapes. Profiles at four of the sites have relatively uniform concentrations in the upper ~0.5 m, with maximum concentrations at or near the ground surface that decline at greater depths (Table 2; Figure 3a-d). At the lowest elevation site on the terminal moraine, the $^{10}Be_{met}$ concentration is greatest at the surface and declines exponentially with depth (Figure 3e). The shallowest profile was at the Copper Creek site, where a coarse, indurated stone layer 60 cm below the ground surface prevented deeper sampling. At Copper Creek the concentration profile is well mixed in the upper 40 cm, exhibits a subsurface peak concentration 40-50 cm below the ground surface, and then declines sharply in the 10 cm interval directly above the stone line, but not to levels as low as those observed in the deepest samples from other profiles (Figure 3a). Inheritance-corrected $^{10}Be_{met}$ inventories range from $1.99x10^{10}$ to $4.92x10^{10}$ atoms cm^{-2} (Table 3), with the largest and smallest inventories at the Copper Creek and East River terminal moraine sites, respectively. Inheritance-corrected F_{met} values range from $1.12x10^6$ to $3.79x10^6$ atom cm^{-2} yr^{-1} (Table 3).

The potential impact of erosion on fluxes varies among the sites (Figure 4). Accounting for the median erosion rate of 0.023 mm yr^{-1} at the Gothic Moraine would increase F_{met} at that site by a factor of 1.8 (Table S2). Assuming the same 0.023 mm yr^{-1} erosion rate, the degree of the erosional impact varies from a minimum factor of 1.3 at the Copper Creek moraine to a maximum of 2.8 at the East River terminal moraine. However, the Gothic Moraine site has the most convex topography of all the sites, with a curvature value of -0.04 m^{-1} and values at the other sites are: -0.03, -0.02, -0.01, and 0 m^{-1} for the Washington Gulch north, East River terminal, Washington Gulch south, and Copper Creek moraines, respectively (Table 1). Hence eq. 4 predicts that erosion rates for the Washington Gulch north, East River terminal, Washington Gulch south sites would be one- to three-quarters of that measured at the Gothic Moraine site, and that the corresponding fluxes would be greater than measured values by factors of 1.8, 1.9, and 1.2, instead of 2.0, 2.8, and 1.7, respectively, if the erosion rate for the Gothic Moraine were assumed. The curvature value of zero at the Copper Creek moraine predicts there is no surface lowering due to erosion, implying the erosion-corrected flux is the same as the measured flux.

F_{met} values are well-correlated with elevation and precipitation metrics in the East River watershed (Figure 5). F_{met} values are linearly and significantly ($p<0.005$) correlated with elevation ($R^2=0.99$), mean annual precipitation ($R^2=0.84-0.90$), mean snow depth in 2018-2019 ($R^2= 0.97$), and mean SWE in 2018-2019 ($R^2=0.97-0.98$). Due to the large range of elevation and precipitation within the watershed (Figure 2), the regression models predict substantial within-watershed variability in F_{met} (Figure 6).

Table 2. $^{10}Be_{met}$ sample information and AMS results.

Site	Sample ID[a] (LLNL BE number)	Sample mass (g)	^{9}Be added as carrier (µg)	$^{10}Be:^{9}Be$ ratio ($x10^{-12}$)	$^{10}Be:^{9}Be$ ratio uncertainty ($x10^{-14}$)	^{10}Be concentration[b] (10^3 atoms g^{-1})	^{10}Be concentration uncertainty (10^3 atoms g^{-1})
Copper Creek	ER_CCT_pit_1_0-10 (BE54737)	0.5227	353.3	12.8	8.50	577993	7878
	ER_CCT_pit_1_10-20	0.5396	352.9	12.5	8.25	546146	7433

	(BE54738)						
	R_ER_CCT_Pit_1_20_30 (BE54926)	0.5174	351.7	11.9	8.08	540389	7405
	ER_CCT_pit_1_30-40 (BE54740)	0.4994	352.9	12.1	11.5	571221	8701
	ER_CCT_pit_1_40-50 (BE54741)	0.4998	352.9	13.5	8.95	636818	8676
	ER_CCT_pit_1_50-60 (BE54743)	0.5004	352.2	6.47	7.15	304159	4941
Washington Gulch North	ER_S2_pit_1_0-10 (BE54729)	0.5456	353.8	13.2	1.16	571850	8461
	ER_S2_pit_1_10-20 (BE54730)	0.5366	353.3	9.09	6.58	399796	5570
	ER_S2_pit_1_20-30 (BE54731)	0.5165	352.2	9.39	6.71	427730	5938
	ER_S2_pit_1_30-40 (BE54732)	0.4948	353.5	8.47	6.13	404217	5631
	ER_S2_pit_1_40-55 (BE54733)	0.4992	353.4	7.19	5.21	339990	4738
	ER_S2_pit_1_55-75 (BE54735)	0.5032	352.4	4.35	4.15	203430	3105
	ER_S2_pit_1_75-95 (BE54736)	0.4959	353.1	2.60	4.82	123570	2725
	ER24_S2_Pit_2_130-145_A (BE55950)	0.5249	351.1	2.40	3.29	107180	1947
Gothic	ER_GM_pit_1_0-15 (BE54756)	0.4996	352.3	7.52	4.88	354209	4802
	ER_GM_pit_1_15-30 (BE54758)	0.4975	350.6	7.89	4.06	371411	4817
	ER_GM_pit_1_30-45 (BE54759)	0.4983	351.9	6.27	5.5	295743	4374
	ER_GM_pit_1_45-65 (BE54760)	0.5025	352.1	3.14	3.65	146885	2446
	ER_GM_pit_1_65-85 (BE54761)	0.5308	354.6	1.82	2.93	90938	1505
	ER_GM_pit_1_85-105 (BE54762)	0.5149	351.3	1.11	1.99	50473	1089
	ER_GM_pit_1_105-125 (BE54765)	0.5073	352.1	2.06	1.81	95406	1413
	ER_GM_pit_1_125-145 (BE54766)	0.5174	351.7	1.79	3.31	81173	1788
Washington Gulch South	ER_AM_Pit_1_0_10 (BE54780)	0.4927	353.0	7.66	6.72	366586	5421
	ER_AM_pit_1_10-20 (BE54750)	0.4863	352.6	7.89	5.23	382133	5207
	ER_AM_pit_1_20-30 (BE54751)	0.5008	352.0	8.21	9.03	385467	6248
	ER_AM_pit_1_30-40 (BE54752)	0.5210	351.8	8.20	8.53	369860	5848
	ER_AM_pit_1_40-55 (BE54753)	0.5648	351.7	8.22	7.34	341913	5088
	ER_AM_pit_1_55-65 (BE54754)	0.5088	352.0	3.05	3.07	140864	2197
	ER_AM_pit_1_65-85 (BE54755)	0.5308	354.6	2.04	2.34	90938	1505
East River Terminal	ER_BCTM_pit_1_0-10 (BE54744)	0.4968	351.1	10.1	7.34	476832	6650
	ER_BCTM_pit_1_10-20 (BE54745)	0.4980	352.2	8.00	7.02	377931	5589
	ER_BCTM_pit_1_20-30 (BE54746)	0.5889	353.0	4.37	3.72	174923	2561

	ER_BCTM_pit_1_30-50 (BE54747)	0.4999	353.0	1.47	1.65	69226	1135
	ER_BCTM_pit_1_50-80 (BE54748)	0.4902	352.9	0.500	9.27	23914	530

[a]Values at the end of each sample ID refer to the sample depth interval (cm). [b]Reported ^{10}Be concentrations are corrected using ^{10}Be:^{9}Be ratios measured in process blanks. ^{10}Be:^{9}Be ratios measured in process blanks in the same batches as the soil samples were: 2.44, 1.64, 2.55, 2.93, 2.11, 2.39, 4.71, 2.92, and 2.70x10^{-15}.

Table 3: Environmental variable values and ^{10}Be$_{met}$ fluxes at each calibration site.

Site	Elevation [a] (m)	MAP [b] (mm yr^{-1})	Mean snow depth[c] 2018 – 2019 (m)	Mean SWE[d] 2018 – 2019 (m)	Uncorrected ^{10}Be$_{met}$ inventory ±1σ uncertainty (10^{10} atoms cm^{-2})	Inheritance-corrected ^{10}Be$_{met}$ inventory ±1σ uncertainty (10^{10} atoms cm^{-2})	Uncorrected ^{10}Be$_{met}$ flux ±1σ uncertainty (10^{6} atoms cm^{-2} yr^{-1})	Inheritance-corrected ^{10}Be$_{met}$ flux ±1σ uncertainty (10^{6} atoms cm^{-2} yr^{-1})
Copper Creek moraine	3462	1353	1.9	0.6	6.04±0.035	4.92±0.036	4.64±0.045	3.79±0.040
Washington Gulch North moraine	2931	784	1.0	0.2	5.64±0.032	3.41±0.033	3.17±0.0400	1.91±0.028
Gothic moraine	2873	885	0.9	0.2	4.64±0.027	2.40±0.028	3.09±0.028	1.60±0.021
Washington Gulch South moraine	2850	655	0.8	0.2	4.45±0.027	2.98±0.027	2.57±0.022	1.72±0.019
East River Terminal moraine	2748	585	0.4	0.1	2.36±0.018	1.99±0.018	1.32±0.018	1.12±0.016

[a] elevation (m) from Wainwright and Williams (2017), [b] mean annual precipitation (MAP) from Mital et al. (2022), (c) mean snow depth (m) from 2018-2019 (Painter, 2018a), and (d) Mean snow water equivalent (SWE) (m) from 2018-2019 (Painter et al., 2018b).

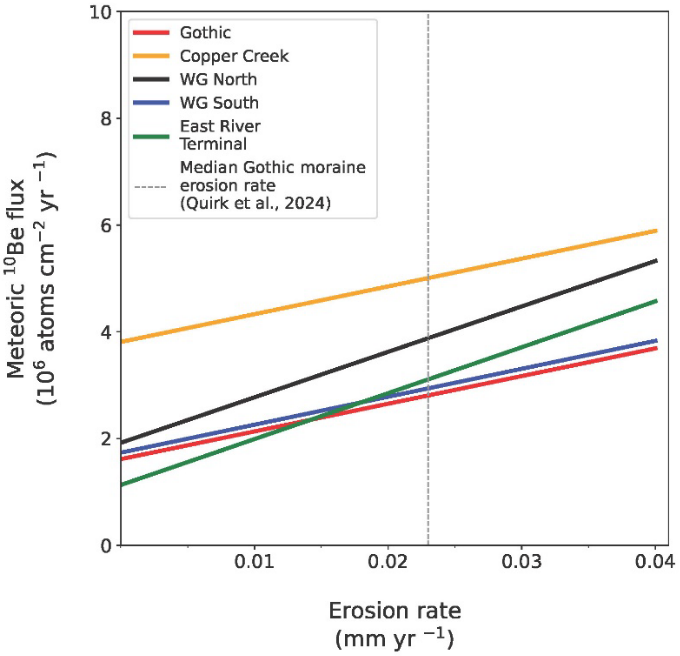

295

Figure 4. Meteoric ^{10}Be flux as a function of erosion rate. The y-intercept is the measured flux based on soil inventories and moraine ages, which does not account for erosion or decay (which has a negligible impact on flux). Predictions for each site have different slopes due to differences in the concentration of $^{10}Be_{met}$ at the soil surface.

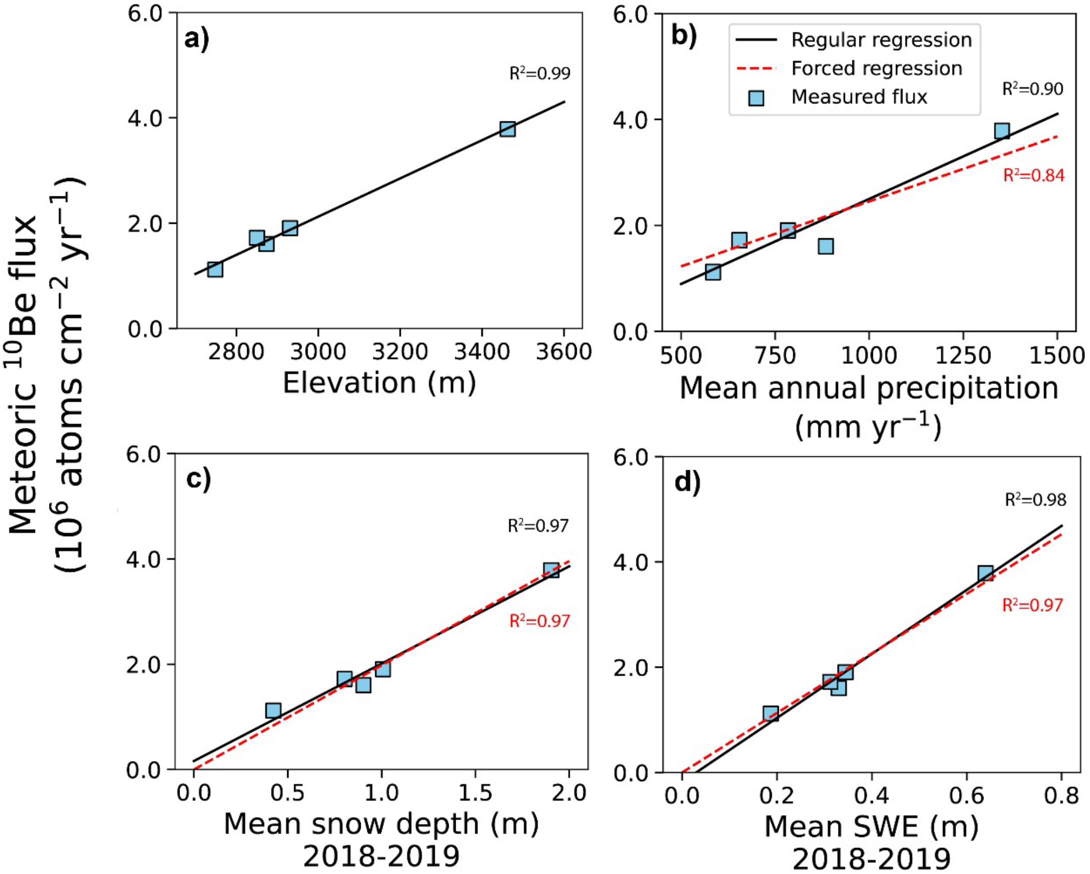

300

Figure 5. Linear regression models of ^{10}Be$_{met}$ flux versus (a) elevation, (b) mean annual precipitation (MAP), (c) mean snow depth (2018–2019), and (d) mean snow water equivalent (SWE) (2018–2019). The black lines show standard regression models and the red dashed lines show regression models where the y-intercept is forced to be zero. For the standard regression models, the elevation model has a slope of 3.63x10^3, y-intercept of –8.76x10^6, R^2 of 0.99, and a p-value of 0.0003. The MAP model has a slope of 3.21x10^3, y-intercept of –7.11x10^5, R^2 of 0.90, and a p-value of 0.01. The mean snow depth model has a slope of 1.85x10^6, y-intercept of 1.62x10^5, R^2 of 0.97, and a p-value of 0.001. The SWE model has a slope of 6.08x10^6, y-intercept of -1.80x10^5, R^2 of 0.98, and a p-value of 0.001. For the forced regression models, the MAP model has a slope of 2.45x10^3, R^2 of 0.84, and a p-value of 0.0002. The average snow depth model has a slope of 1.98x10^6, R^2 of 0.97, and a p-value of 0.00002. The SWE model has a slope of 5.66x10^6, R^2 of 0.97, and a p-value of 0.000007.

The different regression models predicted watershed-averaged F_{met} values that vary by more than a factor of two (Table 3). For elevation, the regression model yields an average F_{met} of 2.66x10^6 atoms cm^{-2} yr^{-1}. The MAP-based regression resulted in average F_{met} values of 1.19x10^6 atoms cm^{-2} yr^{-1} for the standard and 1.46x10^6 atoms cm^{-2} yr^{-1} for the forced regression model, respectively. Snow depth models produced average F_{met} values of 3.52x10^6 and 3.57x10^6 atoms cm^{-2} yr^{-1}for the standard and forced regressions, respectively. Similarly, SWE-based regressions yielded watershed-averaged F_{met} values of 2.65 x10^6 and 2.64x10^6 atoms cm^{-2} yr^{-1} for the standard and forced regressions, respectively. We assessed the influence of extreme values and potential outliers by calculating watershed-averaged F_{met} values using only pixels with the lowest 99th, 95th, and 90th percentile values, which resulted in lower mean F_{met} values (Table 4).

Table 4. Watershed-averaged ^{10}Be$_{met}$ flux predictions based on all pixels (100%) and when excluding pixels with high values by using only the lowest 99, 95, and 90th percentile values when calculating the mean.

Variable	Regression type	Meteoric ^{10}Be flux			
		100% (10^6 atoms cm^{-2} yr^{-1})	**99%** (10^6 atoms cm^{-2} yr^{-1})	**95%** (10^6 atoms cm^{-2} yr^{-1})	**90%** (10^6 atoms cm^{-2} yr^{-1})
Elevation (m)	Regular	2.66	2.56	2.46	2.35
MAP (mm yr^{-1})	Regular	1.23	1.20	1.11	0.99
	Forced	1.48	1.46	1.38	1.30
Mean snow depth (m) 2018 - 2019	Regular	3.55	3.44	3.18	2.96
	Forced	3.62	3.50	3.23	3.00
Mean SWE (m) 2018-2019	Regular	2.83	2.74	2.490	2.27
	Forced	2.80	2.72	2.49	2.28

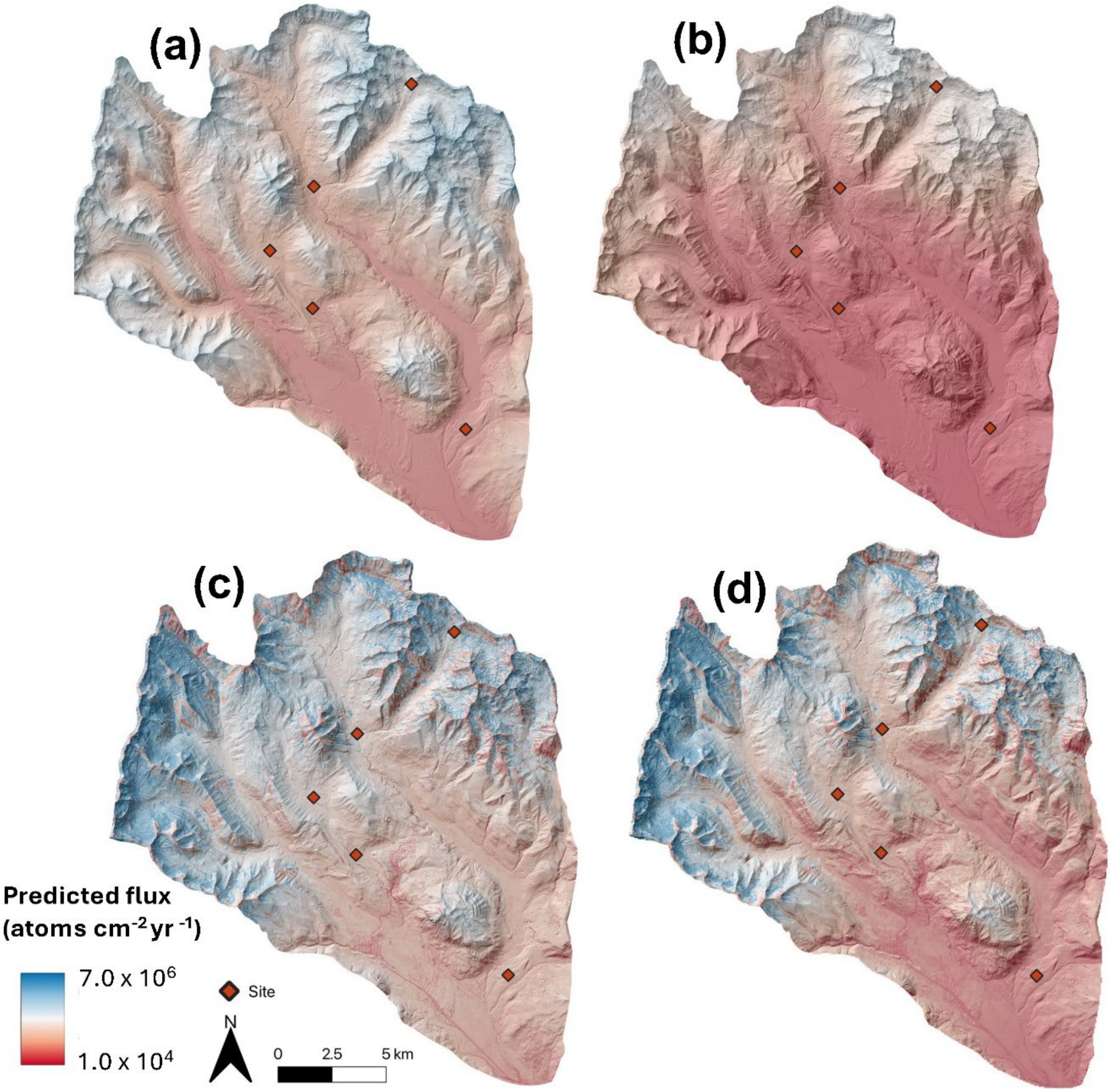

Figure 6. Spatial predictions of ^{10}Be$_{met}$ flux based on regression models using: (a) elevation; (b) mean annual precipitation; (c) mean snow depth from 2018–2019; and (d) mean snow water equivalent from 2018-2019.

5 Discussion

^{10}Be$_{met}$ profiles tend to have characteristic shapes, and the shapes are sometimes used to infer processes of ^{10}Be$_{met}$ mobility (e.g., Graly, 2010). The two most common profile shapes are characterized by either a subsurface peak in concentration or concentrations that decline with depth from a maximum value at the soil surface (Graly, 2010). The profile on the East River terminal moraine exhibits an exponential decline in concentration with depth, however the concentrations at the other four sites are fairly uniform with depth. The uniform profiles likely arise from bioturbation, via vegetation or burrowing mammals. Pocket gophers (*Thomomys talpoides*) are the main soil disturbing mammal within the East River watershed, and soil disturbance can be intense, with surveys indicating soil disturbance by burrowing can exceed one disturbance per m^2 within the elevation range of our sampling sites (Lynn et al., 2018). The distinct stone line at the Copper Creek site may have been generated by bioturbation (e.g., Johnson, 1989), though we cannot rule out the possibility of periglacial origin (Ball, 1967).

Pedogenic loss of $^{10}Be_{met}$ has been documented or suspected in low pH soils with substantial chemical alteration (e.g., Pavich et al., 1984; Bacon et al., 2012; Dixon et al., 2018). The partition coefficient for $^{10}Be_{met}$ is high when pH is greater than ~4.5 (You et al., 1989) but declines at lower pH values. Analysis of a compilation of soil $^{10}Be_{met}$ and pH data suggest loss is most likely to occur below a pH of 3.9 (Graly et al., 2010). The 0-10 cm interval sample at Copper Creek site had the lowest measured pH value of 4.3, but pH increased with depth to a value of 5.4 at the base of the soil profile, and pH values for the other sites are higher. Hence we infer $^{10}Be_{met}$ loss via chemical leaching is minimal and that mobilized $^{10}Be_{met}$ is likely confined within the sampled horizons. Minimal chemical loss of $^{10}Be_{met}$ was also inferred at a site near Pinedale, Wyoming, USA, which has similar-aged moraines and a climate and ecosystem broadly similar to the East River (Clow et al., 2020).

Glacial moraines erode via diffusive soil transport processes (e.g., Putkonen and Swanson, 2003). The F_{met} values we measure are hence minimum values because erosional loss of $^{10}Be_{met}$ reduces inventories. However, our analysis suggests accounting for erosion would increase our F_{met} values by less than a factor of two. Incorporating the median erosion rate for the Gothic Moraine inferred from the $^{10}Be_{in\ situ}$ profile (Quirk et al., 2024) yields a flux that is 1.8 times greater than the measured flux that does not account for erosion. However, curvature data indicate the topography at the other sites has lower convexity than the Gothic moraine site (Table 1), which reduces the influence of erosion (eq. 4). Equations 3 and 4 predict that lower erosion rates at the other sites change fluxes by a factor of one at the Copper Creek site where topographic curvature, and hence erosion rates are zero. Accounting for topographic influences on erosion rates at the other sites predicts that fluxes are 1.2 to 1.9 times higher at the other sites. Because the erosion rates at four of the five calibration sites are unconstrained, we do not use erosion-corrected values when predicting watershed-averaged fluxes, which introduces uncertainty in our F_{met} estimates (Figure 4). Despite potential uncertainty caused by erosion, the F_{met} predictions are strongly correlated with environmental factors.

F_{met} is highly correlated with elevation, MAP, snow depth, and SWE, which is unsurprising because these variables are related to one another via orographic controls on precipitation rates. However, different slope and intercept values for regression relationships result in different F_{met} predictions for the same location and watershed-averaged fluxes that differ by a factor of 2 to 3. The snow depth and SWE datasets cover only two winters, which is only a tiny fraction of the post-glacial period over which ^{10}Be$_{\text{met}}$ has accumulated in soils. Recent snowfall magnitude and spatial patterns may differ from Holocene averages, suggesting predictions from the snow-based variables should be used with caution. However, unlike elevation and MAP datasets, the snow-based inventories yield insight on how local-scale topography may influence spatial patterns of $F_{met.}$ For example, we predict that lower snow accumulation on sharp ridges relative to adjacent slopes leads to lower ^{10}Be$_{\text{met}}$ accumulation on ridges (Figure 6). Watershed-averaged fluxes predicted using snow depth and SWE are more sensitive to extreme values that averages based on elevation and MAP (Table 3). The mean snow depth of 1.9 m at the highest elevation Copper Creek site is a fraction of the highest snow depth values, which exceed 20 m (Figure S4) and are potentially artefacts. The lack of F_{met} calibration sites in areas with higher snow accumulation may result in inaccurate predictions for such areas, however the lack of moraines at higher elevations makes it difficult to measure ^{10}Be$_{\text{met}}$ fluxes in such areas. The MAP data are based on decadal-scale precipitation measurements but are interpolated based on elevation. Elevation is the only parameter not subject to temporal bias. Hence elevation should be a robust predictor of F_{met}, though elevation-based predictions may be biased where local topography leads to persistent snow redistribution via wind and avalanches. Given the different F_{met} predictions from the elevation, MAP, snow depth, and SWE datasets, an ensemble approach may be appropriate for using F_{met} values to quantify surface process rates, in a manner similar to using multiple production rate scaling models when determining ^{10}Be$_{in\ situ}$ exposure ages (e.g., Balco et al., 2008).

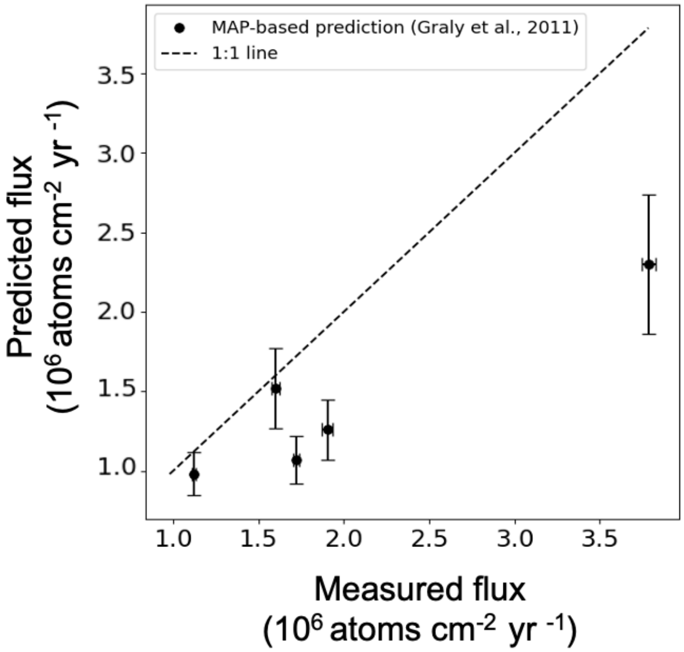

Figure 7. Predicted ^{10}Be$_{\text{met}}$ flux from the empirical precipitation-based model of Graly et al. (2011) versus measured flux values for the five study sites.

Measured fluxes on each of the moraines in the East River watershed are lower than predictions from an empirical precipitation-based model (Graly et al., 2011), by about 10% to 40% (Figure 7). F_{met} values for the two sites with the lowest MAP overlap within uncertainty with predictions from the Graly et al. (2011) model, but fluxes at the sites with greater MAP are underpredicted. If we were to correct the predictions to reflect mean paleomagnetic and solar intensity variability for the Holocene, the Graly et al. (2011) flux predictions would increase (e.g., Clow et al., 2020), which would further increase the difference between the measured and predicted F_{met} values.

GCM-based models predict F_{met} values of 1.01x10^{6} atoms cm^{-2} yr^{-1} (Heikillä and von Blanckenberg, 2015), 1.71x10^{6} atoms cm^{-2} yr^{-1} (Zheng et al., 2024, 200 MeV solar modulation function) and 2.75x10^{6} atoms cm^{-2} yr^{-1} (Zheng et al., 2024, 500 MeV solar modulation function) for the East River watershed and its tributaries (Figure 8). A single grid-cell from the GCM-models covers an area larger than the watershed, hence the models simulate the influence of meso-scale atmospheric dynamics on F_{met}, but do not capture within-watershed F_{met} variability caused by orographic precipitation. The measured F_{met} values and GCM-based predictions vary by nearly a factor of four for the most extreme case. However, because they cover a larger spatial scale, our empirically-predicted watershed-averaged F_{met} values are more directly comparable to the GCM-based predictions than the point-based measurements on each moraine. The watershed-averaged F_{met} value predicted by snow depth is greater than any of the GCM-based predictions (Figure 8). However, the watershed-averaged F_{met} values predicted by elevation (2.66x10^{6} atoms cm^{-2} yr^{-1}) and SWE (2.80–2.83 x10^{6} atoms cm^{-2} yr^{-1}) are similar to the 2.75x10^{6} atoms cm^{-2} yr^{-1} 500 MeV prediction of Zeng et al. (2024) (Figure 8). The MAP-based predictions of 1.23–1.48 x10^{6} atoms cm^{-2} yr^{-1}) are bracketed by the 1.01x10^{6} atoms cm^{-2} yr^{-1} (Heikillä and von Blanckenberg, 2015) and 1.71x10^{6} atoms cm^{-2} yr^{-1} (Zheng et al., 2024, 200 MeV solar modulation function) values, though it is notable that the MAP-based watershed-averaged flux is distinctly lower than the predictions based on elevation, snow depth, and SWE (Figure 8).

Comparing measured F_{met} values against GCM-based predictions is not straightforward due to the likely contribution of dust to the measured values. The contribution of dust to ^{10}Be$_{\mathrm{met}}$ inventories in the East River is unconstrained, but dust fluxes inferred from lacustrine sediment in the nearby San Juan Mountains increased from ~0.01 g cm^{-2} yr^{-1} to 0.4 g cm^{-2} yr^{-1} over the last several centuries (Ballantyne et al., 2011) and recent snowpack measurements indicate seasonal dust fluxes are on the order of 5-10 g cm^{-2} yr^{-1} (Lawrence et al., 2010). Dust fluxes in the Colorado Front Range are 0.1–0.2 g cm^{-2} kyr^{-1} (Dethier et al., 2012). Dust fluxes in the Front Range contribute <10% to the total flux of ^{10}Be$_{\mathrm{met}}$ (Ouimet et al., 2015). If the contribution of dust in the East River is comparable to that in the Front Range, accounting for dust would not substantially influence the magnitude of discrepancies between GCM-based predictions and our empirically derived F_{met} estimates.

At a regional level, F_{met} values for the Colorado Front Range based on soil inventories have been estimated to be 1.5±0.2 x10^{6} atoms cm^{-2} yr^{-1} (Ouimet et al., 2015). Soil inventory-based F_{met} values in the Wind River Mountains, Wyoming are 1.46±0.20×10^{6} atoms cm^{-2} yr^{-1} and 1.30±0.48×10^{6} atoms cm^{-2} yr^{-1} for Pinedale- and Bull Lake-aged moraines, respectively

(Clow et al., 2020). The 1.12–3.79 x10^6 atoms cm^{-2} yr^{-1} F_{met} values we measure are consistent with those from the Front Range and Wind River Mountains, though those sites are drier, with ~500 mm yr^{-1} of mean annual precipitation in the Front Range (Ouimet et al., 2015) and 276 mm yr^{-1} at the Wind River Mountains sites (Clow et al., 2020), relative to the 590 to 1350 mm yr^{-1} precipitation at the five East River study sites. The driest site in the East River (terminal moraine, 590 mm yr^{-1} MAP) has a measured F_{met} of 1.12 x10^6 atoms cm^{-2} yr^{-1}, which is lower than fluxes inferred in the Front Range and Wind River Mountains. Accounting for erosion would nearly double the measured F_{met} value measured at the East River terminal moraine, which would result in higher F_{met} for the East River relative to comparable sites in the Front Range and Wind River Mountains.

Local calibration of F_{met} greatly increases the utility of ^{10}Be$_{\mathrm{met}}$ as a tracer of surface processes in the East River watershed, where there is prevalent shale bedrock that is not amenable to the more common ^{10}Be$_{in\ situ}$ method. Our findings show that, whereas F_{met} predictions from GCM-based models may be broadly applicable for large-scale watershed applications, such models are unable to capture the high spatial variability in F_{met} that is driven by orographic influences on precipitation. Hence using ^{10}Be$_{\mathrm{met}}$ to quantify physical erosion and weathering rates at the small watershed or soil profile-scale requires not only local-scale calibration of F_{met}, but also a means for predicting F_{met} for sites where elevation and precipitation varies from that of the sites used to calibrate F_{met}. Our study demonstrates how high-resolution LiDAR elevation and snowpack datasets can be combined with locally calibrated F_{met} measurements to generate spatially resolved F_{met} predictions, which furthers our understanding of the processes that control the delivery of ^{10}Be$_{\mathrm{met}}$ to soils.

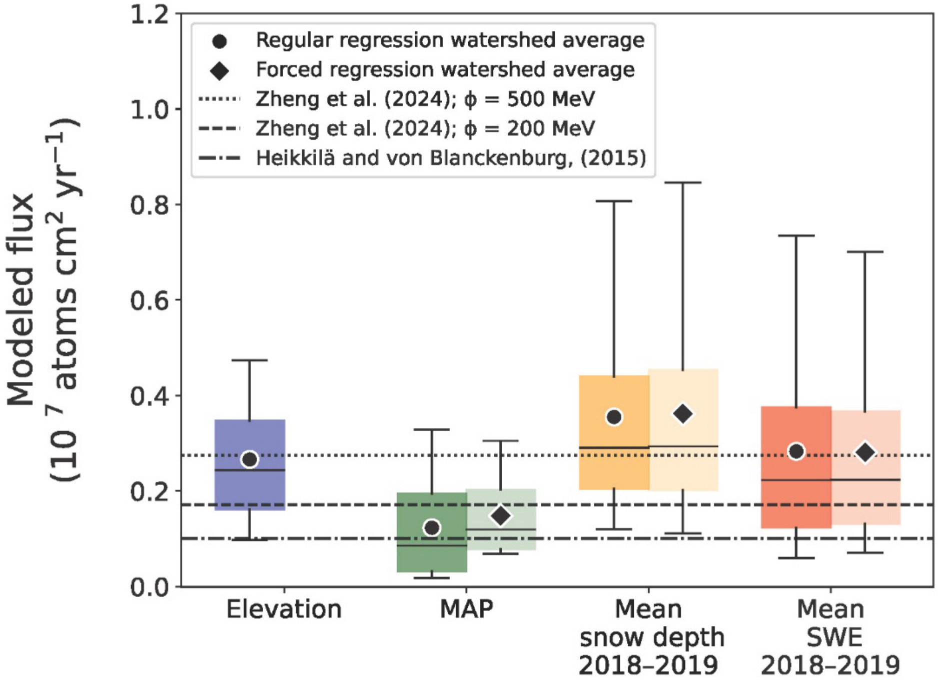

https://doi.org/10.5194/egusphere-2025-4254
Preprint. Discussion started: 5 September 2025

Figure 8: Watershed-scale $^{10}Be_{met}$ fluxes predicted by empirical models based on elevation, mean annual precipitation (MAP), mean snow depth, and mean SWE and flux predictions from global circulation-based (GCM) models. Boxplots show the median (horizontal line), interquartile range, and 5th and 95th percentile flux values. Mean fluxes are show with circles (standard regression models, left box) and diamonds (forced regression models, right box). GCM-based flux predictions from Heikkilä and von Blanckenburg (2015) and Zheng et al. (2024) are shown as horizontal lines.

6 Conclusions

Meteoric ^{10}Be fluxes calculated from soil inventories on five glacial moraines dated to 13.0–17.9 ka in the East River watershed, Colorado, USA range from 1.12–3.79×10^{6} atoms cm^{-2} yr^{-1}. Soil pH values are above the threshold where loss of meteoric ^{10}Be via leaching is likely to occur. The fluxes are not corrected for loss of ^{10}Be atoms due to erosion, since the erosion rate is constrained for only one of the moraines, but our analyses indicate fluxes may be 1.2 to 1.9 times higher than measured values due to erosion. The measured fluxes vary systematically with environmental gradients across the watershed and are highly correlated (R^2=0.84–0.99) with elevation, mean annual precipitation, mean snow depth, and mean snow water equivalent, reflecting the important role orographic precipitation plays in influencing spatial patterns of meteoric ^{10}Be flux within the watershed. Elevation is the only predictor of flux that is not subject to temporal bias, whereas the snow-based predictions are based on only two years of measurements, and the magnitude and pattern of snow accumulation during those years may vary substantially from Holocene averages. However, the snow-based predictions yield insight into smaller-scale topographic controls on meteoric ^{10}Be fluxes, such as predictions of lower fluxes on sharp ridge crests relative to adjacent hillslopes due to snow redistribution. The fluxes measured at the five moraines are lower than predictions from an empirical model relating flux and mean annual precipitation (Graly et al., 2011). Watershed-averaged fluxes predicted from empirical correlations between measured flux and elevation, mean annual precipitation, mean snow depth, and mean snow water equivalent range from 1.23–3.62×10^{6} atoms cm^{-2} yr^{-1}, some of which are comparable to predictions from global-scale general circulation models, which are 1.01×10^{6} atoms cm^{-2} yr^{-1} (Heikillä and von Blanckenberg, 2015), 1.71x10^{6} atoms cm^{-2} yr^{-1}, and 2.75x10^{6} atoms cm^{-2} yr^{-1} (Zheng et al., 2024), though these models do not capture the spatial variation in flux within the watershed. The findings highlight the high degree which meteoric ^{10}Be fluxes vary within alpine landscapes and demonstrate how combining soil meteoric ^{10}Be inventories and high-resolution gridded datasets can generate spatially resolved meteoric ^{10}Be flux predictions. Our results enhance the utility of meteoric ^{10}Be as a tracer of surface processes in the East River watershed, and other alpine landscapes with rocks that are not conducive to using *in situ*-produced ^{10}Be and add to our overall understanding of the factors that influence the delivery and retention of meteoric ^{10}Be in soils.

7 Data availability

Data are available at the U.S. Department of Energy ESS-DIVE archive: Marmolejo-Cossío J; Larsen I; Hidy A (2025): Meteoric beryllium-10 fluxes from soil inventory measurements in the East River watershed, Colorado, USA. Abiotic and Biotic Controls on Chemical Weathering Rates and Solute Generation. Dataset. doi:10.15485/2586513 [Note data repository submission will be made public following pending review by ESS-DIVE staff]

8 Author contribution

Marmolejo: data curation, formal analysis, investigation, writing (original draft preparation)

Larsen: conceptualization, funding acquisition, investigation, methodology, project administration, resources, supervision, writing (original draft preparation, reviewing and editing)

Hidy: formal analysis, writing (reviewing and editing)

9 Competing interests

The authors declare that they have no conflict of interest.

10 Acknowledgments

We thank J. Reithel at the Rocky Mountain Biological Laboratory for securing access to study sites, B. Quirk for assistance sampling, J. Deems for information on snow datasets, and M. Winnick for use of a pH probe. This work was supported by U.S. Department of Energy grant DE-SC0020354 to Larsen. Prepared in part by LLNL under Contract DE-AC52-07NA27344. This is LLNL-JRNL-2007359.

11 References

Bacon, A.R., Richter, D.D., Bierman, P.R. and Rood, D.H., 2012. Coupling meteoric 10Be with pedogenic losses of 9Be to improve soil residence time estimates on an ancient North American interfluve. Geology, 40(9), pp.847-850.

Ball, D.F., 1967. Stone pavements in soils of Caernarvonshire, North Wales. *Journal of Soil Science*, *18*(1), pp.103-108.

Balco, G., Stone, J.O., Lifton, N.A. and Dunai, T.J., 2008. A complete and easily accessible means of calculating surface exposure ages or erosion rates from 10Be and 26Al measurements. Quaternary geochronology, 3(3), pp.174-195.

Ballantyne, A.P., Brahney, J., Fernandez, D., Lawrence, C.L., Saros, J., Neff, J.C., 2011. Biogeochemical response of alpine lakes to a recent increase in dust deposition in the Southwestern US. Biogeosciences 8 (9), 2689e2706. http://dx.doi.org/10.5194/bg-8-2689-2011.

Bierman PR, Nichols KK. 2004. Rock to sediment – slope to sea with 10Be – rates of landscape change. Annual Review of Earth and Planetary Science 32: 215–255. DOI: 10.1146/annurev.earth.32.101802.120539

Borchers, B., Marrero, S., Balco, G., Caffee, M., Goehring, B., Lifton, N., Nishiizumi, K., Phillips, F., Schaefer, J. and Stone, J., 2016. Geological calibration of spallation production rates in the CRONUS-Earth project. *Quaternary Geochronology*, *31*, pp.188-198.

Brown, L. (1984). Applications of Accelerator Mass Spectrometry. Annual Review of Earth and Planetary Sciences, 12(1), 39–59. https://doi.org/10.1146/ANNUREV.EA.12.050184.000351

Brown, L., Pavich, M.J., Hickman, R.E., Klein, J. and Middleton, R., 1988. Erosion of the eastern United States observed with 10Be. Earth Surface Processes and Landforms, 13(5), pp.441-457.

Brown, L., Stensland, G.J., Klein, J., Middleton, R., 1989. Atmospheric deposition of ^{7}Be and ^{10}Be. Geochimica et Cosmochimica Acta 53,135}142.

Brown, L. (1987b). 10Be as a tracer of erosion and sediment transport. Chemical Geology: Isotope Geoscience Section, 65(3–4), 189–196. https://doi.org/10.1016/0168-9622(87)90002-9

Brown, L., (1987a). 10Be: Recent applications in Earth sciences. Philosophical Transactions of the Royal Society of London. Series A, Mathematical and Physical Sciences, 323(1569), pp.75-86

Campforts, B., Vanacker, V., Vanderborght, J., Baken, S., Smolders, E. and Govers, G., 2016. Simulating the mobility of meteoric 10Be in the landscape through a coupled soil-hillslope model (Be2D). Earth and planetary science letters, 439, pp.143-157

Chmeleff, J., von Blanckenburg, F., Kossert, K. and Jakob, D., 2010. Determination of the 10Be half-life by multicollector ICP-MS and liquid scintillation counting. Nuclear Instruments and Methods in Physics Research Section B: Beam Interactions with Materials and Atoms, 268(2), pp.192-199.

Clow, T., Willenbring, J. K., Schaller, M., Blum, J. D., Christl, M., Kubik, P. W., & von Blanckenburg, F. (2020). Calibrating a long-term meteoric 10Be delivery rate into eroding western US glacial deposits by comparing meteoric and in situ produced 10Be depth profiles. Geochronology, 2(2), 411–423. https://doi.org/10.5194/GCHRON-2-411-202

Daly, C., Halbleib, M., Smith, J. I., Gibson, W. P., Doggett, M. K., Taylor, G. H., Curtis, J., and Pasteris, P. P.: Physiographically sensitive mapping of climatological temperature and precipitation across the conterminous United States, Int. J. Climatol., 28, 2031–2064, https://doi.org/10.1002/joc.1688, 2008.

Dannhaus, N., Wittmann, H., Krám, P., Christl, M. and von Blanckenburg, F., 2018. Catchment-wide weathering and erosion rates of mafic, ultramafic, and granitic rock from cosmogenic meteoric 10Be/9Be ratios. Geochimica et Cosmochimica Acta, 222, pp.618-641.

Deng, K., Wittmann, H., & von Blanckenburg, F. (2020b). The depositional flux of meteoric cosmogenic 10Be from modeling and observation. Earth and Planetary Science Letters, 550, 116530. https://doi.org/10.1016/J.EPSL.2020.116530

Deng, K., Yang, S., von Blanckenburg, F., & Wittmann, H. (2020a). Denudation Rate Changes Along a Fast-Eroding Mountainous River With Slate Headwaters in Taiwan From 10Be (Meteoric)/9Be Ratios. Journal of Geophysical Research: Earth Surface, 125(2), e2019JF005251. https://doi.org/10.1029/2019JF005251

Deng, K., Wittmann, H., Yang, S. and von Blanckenburg, F., 2021. The upper limit of denudation rate measurement from cosmogenic 10Be (meteoric)/9Be ratios in Taiwan. Journal of Geophysical Research: Earth Surface, 126(10), p.e2021JF006221.

Dethier, D.P., Birkeland, P.W., McCarthy, J.A., 2012. Using the accumulation of CBD- extractable iron and clay content to estimate soil age on stable surfaces and nearby slopes, Front Range, Colorado. Geomorphology. http://dx.doi.org/10.1016/j.geomorph.2012.05.022.

Dixon, J.L., Chadwick, O.A. and Pavich, M.J., 2018. Climatically controlled delivery and retention of meteoric ^{10}Be in soils. *Geology*, *46*(10), pp.899-902.

Dühnforth, M., Anderson, R.S., Ward, D.J. and Blum, A., 2012. Unsteady late Pleistocene incision of streams bounding the Colorado Front Range from measurements of meteoric and in situ 10Be. Journal of Geophysical Research: Earth Surface, 117(F1).

Egli, M., Brandová, D., Böhlert, R., Favilli, F., & Kubik, P. W. (2010). 10Be inventories in Alpine soils and their potential for dating land surfaces. Geomorphology, 119(1–2), 62–73. https://doi.org/10.1016/J.GEOMORPH.2010.02.019

Field, C. v., Schmidt, G. A., Koch, D., & Salyk, C. (2006). Modeling production and climate-related impacts on 10Be concentration in ice cores. Journal of Geophysical Research: Atmospheres, 111(D15). https://doi.org/10.1029/2005JD006410

Foster, M.A., Anderson, R.S., Wyshnytzky, C.E., Ouimet, W.B. and Dethier, D.P., 2015. Hillslope lowering rates and mobile-regolith residence times from in situ and meteoric 10Be analysis, Boulder Creek Critical Zone Observatory, Colorado. Bulletin, 127(5-6), pp.862-878.

Gaskill, D.L., Godwin, L.H., Mutschler, F.E., 1967. Geologic map of the Oh-Be-Joyful quadrangle, Gunnison County, Colorado, scale 1:24,000. US Geological Survey, Geologic Quadrangle 578. https://doi.org/10.3133/gq578.

Gaskill, D.L., Mutschler, F.E., Kramer, J.H., Thomas, J.A., Zahony, G., 1991. Geologic map of the Gothic quadrangle, Gunnison County, Colorado, scale 1:24,000. US Geological Survey Geologic Quadrangle 1689. https://doi.org/10.3133/gq1689.

Gosse, J.C. and Phillips, F.M., 2001. Terrestrial in situ cosmogenic nuclides: theory and application. Quaternary Science Reviews, 20(14), pp.1475-1560.

Graham, I., et al. (2003), Atmospheric deposition of 7Be and 10Be in New Zealand rain (1996–98), Geochim. Cosmochim. Acta, 67(3), 361–373, doi:10.1016/S0016-7037(02)01092-X.

Graly, J. A., Bierman, P. R., Reusser, L. J., & Pavich, M. J. (2010). Meteoric 10Be in soil profiles – A global meta-analysis. Geochimica et Cosmochimica Acta, 74(23), 6814–6829. https://doi.org/10.1016/J.GCA.2010.08.036

Harden, J. W., T. L. Fries, and M. J. Pavich (2002), Cycling of beryllium and carbon through hillslope soils in Iowa, Biogeochemistry, 60, 317–335.

Harte, J., and Shaw, R. 1995. Shifting dominance within a montane vegetation community: results of a climate-warming experiment. Science, 267, 876–880.

Heikkilä, U. and Von Blanckenburg, F., 2015. The global distribution of Holocene meteoric 10Be fluxes from atmospheric models: Distribution maps for terrestrial Earth's surface applications. GFZ Data Services, 10.

Hubbard, S. S., Williams, K. H., Agarwal, D., Banfield, J., Beller, H., Bouskill, N., Brodie, E., Carroll, R., Dafflon, B., Dwivedi, D., Falco, N., Faybishenko, B., Maxwell, R., Nico, P., Steefel, C., Steltzer, H., Tokunaga, T., Tran, P. A., Wainwright, H., … Steltzer, H. (2018). The East River, Colorado, Watershed: A Mountainous Community Testbed for Improving Predictive Understanding of Multiscale Hydrological-Biogeochemical Dynamics Special Section: Hydrological Observatories. Vadose Zone Journal | Advancing Critical Zone Science. https://doi.org/10.2136/vzj2018.03.0061

Johnson, D.L., 1989. Subsurface stone lines, stone zones, artifact-manuport layers, and biomantles produced by bioturbation via pocket gophers (Thomomys bottae). *American Antiquity*, *54*(2), pp.370-389.

Jordan, C. E., Dibb, J. E., & Finkel, R. C. (2003). <supscr>10</supscr>Be/<supscr>7</supscr>Be tracer of atmospheric transport and stratosphere-troposphere exchange. J. Geophys. Res, 108(D8), 4234. https://doi.org/10.1029/2002JD002395

Jungers, M. C., Bierman, P. R., Matmon, A., Nichols, K., Larsen, J., and Finkel, R.: Tracing hillslope sediment production and transport with in situ and meteoric 10Be, J. Geophys. Res.-Earth, 114, F04020, https://doi.org/10.1029/2008JF001086, 2009.

Korschinek, G., Bergmaier, A., Faestermann, T., Gerstmann, U.C., Knie, K., Rugel, G., Wallner, A., Dillmann, I., Dollinger, G., Von Gostomski, C.L. and Kossert, K., 2010. A new value for the half-life of 10Be by heavy-ion elastic recoil detection and liquid scintillation counting. Nuclear Instruments and Methods in Physics Research Section B: Beam Interactions with Materials and Atoms, 268(2), pp.187-191.

Krone, L. V., Wittmann, H., & von Blanckenburg, F. (2024). Precipitation control on weathering intensity and depositional flux of Meteoric 10Be revealed from soil profiles along a climate gradient (Chile). Geophysical Research Letters, 51(15), e2024GL108825. https://doi.org/10.1029/2024GL108825

Kwang, J.S., Thaler, E.A., Quirk, B.J., Quarrier, C.L. and Larsen, I.J., 2022. A landscape evolution modeling approach for predicting three-dimensional soil organic carbon redistribution in agricultural landscapes. Journal of Geophysical Research: Biogeosciences, 127(2), p.e2021JG006616.

Lal, D. and Peters, B., 1967. Cosmic ray produced radioactivity on the Earth. In Kosmische strahlung II/cosmic rays II (pp. 551-612). Berlin, Heidelberg: Springer Berlin Heidelberg.

Lawrence, C.R., Painter, T.H., Landry, C.C. and Neff, J.C., 2010. Contemporary geochemical composition and flux of aeolian dust to the San Juan Mountains, Colorado, United States. *Journal of Geophysical Research: Biogeosciences*, *115*(G3).

Lynn, J.S., Canfield, S., Conover, R.R., Keene, J. and Rudgers, J.A., 2018. Pocket gopher (Thomomys talpoides) soil disturbance peaks at mid-elevation and is associated with air temperature, forb cover, and plant diversity. Arctic, Antarctic, and Alpine Research, 50(1), p.e1487659.

Mackey, B.H., Roering, J.J. and McKean, J.A., 2009. Long-term kinematics and sediment flux of an active earthflow, Eel River, California. Geology, 37(9), pp.803-806.

Masarik, J., & Beer, J. (1999). Simulation of particle fluxes and cosmogenic nuclide production in the Earth's atmosphere. Journal of Geophysical Research Atmospheres, 104(D10), 12099–12111. https://doi.org/10.1029/1998JD200091

McHargue, L.R. and Damon, P.E., 1991. The global beryllium 10 cycle. Reviews of Geophysics, 29(2), pp.141-158.
McKean, J.A., Dietrich, W.E., Finkel, R.C., Southon, J.R. and Caffee, M.W., 1993. Quantification of soil production and downslope creep rates from cosmogenic 10Be accumulations on a hillslope profile. Geology, 21(4), pp.343-346.Jagercikova,

Mital, U., Dwivedi, D., Brown, J., and Steefel, C., Downscaled hyper-resolution (400 m) gridded datasets of daily precipitation and temperature (2008–2019) for the East–Taylor subbasin (western United States). United States: N. p., 2022. Web. doi:10.5194/essd-14-4949-2022.

Monaghan, M.C., Krishnaswami, S. and Thomas, J.H., 1983. 10Be concentrations and the long-term fate of particle-reactive nuclides in five soil profiles from California. Earth and Planetary Science Letters, 65(1), pp.51-60.

Monaghan, M.C., Krishnaswami, S. and Turekian, K.K., 1986. The global-average production rate of10Be. Earth and Planetary Science Letters, 76(3-4), pp.279-287.

Monaghan, M.C., McKean, J., Dietrich, W. and Klein, J., 1992. 10Be chronometry of bedrock-to-soil conversion rates. Earth and Planetary Science Letters, 111(2-4), pp.483-492.

Mudd, S.M., Attal, M., Milodowski, D.T., Grieve, S.W. and Valters, D.A., 2014. A statistical framework to quantify spatial variation in channel gradients using the integral method of channel profile analysis. *Journal of Geophysical Research: Earth Surface*, *119*(2), pp.138-152.

Nishiizumi, K., Imamura, M., Caffee, M.W., Southon, J.R., Finkel, R.C. and McAninch, J., 2007. Absolute calibration of 10Be AMS standards. Nuclear Instruments and Methods in Physics Research Section B: Beam Interactions with Materials and Atoms, 258(2), pp.403-413.

Ouimet, W., Dethier, D., Bierman, P., Wyshnytzky, C., Shea, N., & Rood, D. H. (2015). Spatial and temporal variations in meteoric 10Be inventories and long-term deposition rates, Colorado Front Range. Quaternary Science Reviews, 109, 1–12. https://doi.org/10.1016/J.QUASCIREV.2014.11.003

Painter, T. (2018a). ASO L4 Lidar Snow Depth 3m UTM Grid. (ASO_3M_SD, Version 1). [Data Set]. Boulder, Colorado USA. NASA National Snow and Ice Data Center Distributed Active Archive Center. https://doi.org/10.5067/KIE9QNVG7HP0. Date Accessed 05-12-2025.

Painter, T. (2018b). ASO L4 Lidar Snow Water Equivalent 50m UTM Grid. (ASO_50M_SWE, Version 1). [Data Set]. Boulder, Colorado USA. NASA National Snow and Ice Data Center Distributed Active Archive Center. https://doi.org/10.5067/M4TUH28NHL4Z. Date Accessed 05-12-2025.

Pavich, M. J., Brown, L., Klein, J., & Middleton, R. (1984). 10Be accumulation in a soil chronosequence. Earth and Planetary Science Letters, 68(2), 198–204. https://doi.org/10.1016/0012-821X(84)90151-1

Panovska, S., Poluianov, S., Gao, J., Korte, M., Mishev, A., Shprits, Y. Y., & Usoskin, I. (2023). Effects of global geomagnetic field variations over the past 100,000 years on cosmogenic radionuclide production rates in the Earth's atmosphere. Journal of Geophysical Research: Space Physics, 128(8), e2022JA031158. https://doi.org/10.1029/2022JA031158

Portenga, E.W., Bierman, P.R., Trodick, C.D., Greene, S.E., DeJong, B.D., Rood, D.H. and Pavich, M.J., 2019. Erosion rates and sediment flux within the Potomac River basin quantified over millennial timescales using beryllium isotopes. GSA Bulletin, 131(7-8), pp.1295-1311.

Prather, R.M., Underwood, N., Dalton, R.M., Barr, B. and Inouye, B.D., 2023. Climate data from the Rocky Mountain Biological Laboratory (1975–2022). Ecology, 104(11), p.e4153.

Putkonen, J. and Swanson, T., 2003. Accuracy of cosmogenic ages for moraines. *Quaternary Research*, *59*(2), pp.255-261.

Quirk, B.J., Larsen, I.J. and Hidy, A.J., 2024. Latest Pleistocene glacial chronology and paleoclimate reconstruction for the East River watershed, Colorado, USA. Quaternary Research, pp.1-13.

Raisbeck, G., Yiou, F., Fruneau, M. *et al.* Cosmogenic ^{10}Be concentrations in Antarctic ice during the past 30,000 years. *Nature* **292**, 825–826 (1981). https://doi.org/10.1038/292825a0

Reusser, L., Graly, J., Bierman, P., & Rood, D. (2010). Calibrating a long-term meteoric 10Be accumulation rate in soil. Geophysical Research Letters, 37(19). https://doi.org/10.1029/2010GL04475

Stone, J. & Balco, G. Extraction of beryllium-10 from soil by fusion. University of Washington Cosmogenic Nuclide Laboratory. 6 p.

Stone, J.O.H., 1998. A rapid fusion method for separation of beryllium-10 from soils and silicates. Geochimica et Cosmochimica Acta 62 (3), 555}561.

Tsai, H., Maejima, Y. and Hseu, Z.Y., 2008. Meteoric 10Be dating of highly weathered soils from fluvial terraces in Taiwan. Quaternary International, 188(1), pp.185-196.

von Blanckenburg, F., Bouchez, J., & Wittmann, H. (2012). Earth surface erosion and weathering from the 10Be (meteoric)/9Be ratio. Earth and Planetary Science Letters, 351–352, 295–305. https://doi.org/10.1016/J.EPSL.2012.07.022

von Blanckenburg, F. and Bouchez, J., 2014. River fluxes to the sea from the ocean's 10Be/9Be ratio. Earth and Planetary Science Letters, 387, pp.34-43.

Wainwright, H., and Williams, K. 2017. LiDAR collection in August 2015 over the East River Watershed, Colorado, USA. ESS-DIVE. doi:10.21952/WTR/1412542, version: ess-dive-11cf2e833d7443c-20230504T210936015906.

Willenbring, J. K., & von Blanckenburg, F. (2010). Meteoric cosmogenic Beryllium-10 adsorbed to river sediment and soil: Applications for Earth-surface dynamics. Earth-Science Reviews, 98(1–2), 105–122. https://doi.org/10.1016/J.EARSCIREV.2009.10.008

You, C.F., Lee, T. and Li, Y.H., 1989. The partition of Be between soil and water. Chemical Geology, 77(2), pp.105-118.

Zheng, M., Adolphi, F., Ferrachat, S., Mekhaldi, F., Lu, Z., Nilsson, A. and Lohmann, U., 2024. Modeling atmospheric transport of cosmogenic radionuclide 10Be using geos-chem 14.1. 1 and echam6. 3-ham2. 3: Implications for solar and geomagnetic reconstructions. *Geophysical Research Letters*, *51*(2), p.e2023GL106642.